Optical Materials 165 (2025) 117161

Contents lists available at ScienceDirect

Optical Materials

journal homepage: www.elsevier.com/locate/optmat

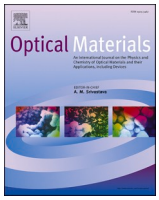

Fe-dependent optical properties of peralkaline soda aluminosilicate glasses: a combined Raman and photoluminescence study

Michele Cassetta [a,b], Anna Safonova [a,c], Gino Mariotto [a], Nicola Daldosso [a], Shujie You [d], Pawan Kumar [d], Alberto Vomiero [d,e], Mohamed Yousri Ben Zaied [a,f], Mongi Bouaicha [f], Francesco Enrichi [a,*]

[a] Department of Engineering for Innovation Medicine and INSTM, University of Verona, Strada le Grazie 15, 37134, Verona, Italy
[b] Department of Earth Sciences University of Torino, I-1012 5, Torino, Italy
[c] Department of Diagnostics and Public Health, University of Verona, Strada le Grazie 15, 37134, Verona, Italy
[d] Department of Engineering Sciences and Mathematics, Luleå University of Technology, 97187, Luleå, Sweden
[e] Department of Molecular Sciences and Nanosystems, Ca- Foscari University of Venice, 30172, Venice, Italy
[f] Faculté des Sciences de Tunis, Université de Tunis El Manar, Laboratoire de Photovoltaique, Centre de Recherches et des Technologies de l'Energie, Technopole de Borj-Cedria, BP 95, Hammam-Lif, Tunis, 2050, Tunisia

ARTICLE INFO

Keywords:
Iron
Fe^{3+}
Silicate glasses
Raman
Photoluminescence

ABSTRACT

This study investigates the influence of iron on the optical properties of peralkaline soda aluminosilicate glasses (NASF), focusing on the interplay between glass structure and optical behavior. Fe doping significantly affects the glass network, altering both its structural connectivity and optical properties. Raman spectroscopy reveals that Fe modifies the glass structure by increasing non-bridging oxygens (NBOs), reducing network connectivity. For the highest FeO_{tot} concentration of 8.2 at.%, a more polymerized structural reorganization occurs due to iron self-compensation. Optical analysis shows that Fe incorporation increases the optical absorption and shifts the absorption edge to higher wavelengths. Tauc plot calculations reveal a decrease in the optical bandgap from 4.0 to 3.2 eV, while the Urbach energy indicates an increase of structural disorder. The photoluminescence (PL) excitation and emission related to Fe^{3+} energy levels is observed, with a broad red emission peak at 700 nm, decreasing with Fe concentration in relation to higher defectivity and clustering. A detailed lifetime analysis shows long lasting tails of the order of milliseconds, also decreasing with Fe content due to non-radiative recombinations and quenching.

1. Introduction

Optical glasses are fundamental pillars of optics and photonics technologies. In the last 50 years significant efforts have been devoted to their developments obtaining considerable progress towards applications, with a very long list of areas such as lighting [1,2], lasers [3], optical fibers [4] and waveguides [5,6], optical amplifiers [7], optical storage devices [8], optical switching [9] and optical limiting materials [10], photochromic [11] and photosensitive glasses [12], magneto optical glasses [13], as well as solar concentrators [14] and spectral conversion films [15–21]. A detailed review of the state of the art and future perspectives in all these areas was recently provided by W. Blanc et al. [22]. A key-factor towards specific properties and applications is that the electrical, optical, mechanical and physical properties of glasses can be tailored by modifying the glass composition and by adding specific dopants even in low concentrations. The addition of transition metals can modify the absorption edge and the optical bandgap, resulting in photoluminescence emission and shifting the material properties from insulating to semiconducting [23–25].

This paper deals with iron-doped soda aluminosilicate glasses (NASF), which are of particular interest in both fundamental research and technological applications including optical materials, functional coatings, and geological processes [26–28]. The presence of iron in the glass network introduces complex interactions between its oxidation state, structural role, and optical response, making it a key component in tailoring the material performance [29–34].

This article is part of a special issue entitled: 80th birthday of Giancarlo C. Righini published in Optical Materials.

* Corresponding author.
E-mail address: francesco.enrichi@univr.it (F. Enrichi).

https://doi.org/10.1016/j.optmat.2025.117161
Received 31 March 2025; Received in revised form 6 May 2025; Accepted 14 May 2025
Available online 15 May 2025
0925-3467/© 2025 The Authors. Published by Elsevier B.V. This is an open access article under the CC BY license (http://creativecommons.org/licenses/by/4.0/).

Iron in silicate glasses exists primarily in two oxidation states, Fe^{2+} and Fe^{3+}. Fe^{3+} usually acts as a network former, contributing to the connectivity of the silicate structure, whereas Fe^{2+} behaves as a network modifier, breaking silicate bonds and increasing the number of non-bridging oxygens. The ratio Fe^{2+}/Fe^{3+} is highly dependent on glass composition, melting conditions, and cooling rates. Understanding this balance is essential for optimizing the optical properties of iron-containing glasses.

In a previous paper, Ref. [31], we synthesized a set of NASF samples with varying Fe content, describing their detailed preparation and characterization and focusing on the correlation between iron oxidation state and glass transition behavior. However, the microstructure and medium-range order (MRO) play a fundamental role as well in defining the optical performance of NASF glasses. These aspects will be the focus of the present work. While short-range order (SRO) provides information on local coordination environments, MRO determines how structural units organize beyond the first coordination shell, influencing light absorption, scattering phenomena, and overall transparency. The presence of iron clusters (of isolated Fe^{3+} ions, along with Fe^{3+}–O^{2+}– Fe^{3+} and Fe^{3+}–O^{2+}– Fe^{2+}) or the occurrence of phase separation at the nanoscale can introduce absorption bands in the visible and near-infrared regions, affecting the coloration and luminescence properties of the glass [35,36]. This study aims to investigate the correlation between the structural arrangement of NASF glasses at different length scales and their optical properties.

2. Experimental

Peralkaline soda-alumina silicate (NASF) glasses were synthesized as described and characterized in Ref. [31]. Six glasses with varying FeO_{tot} content (0–13.9 wt%) were synthesized by melting high-purity reagents at 1600 °C, quenched on a copper plate, and air-cooled. Chemical compositions were determined using electron microprobe analysis, and densities were measured by a helium pycnometer. Iron oxidation states and coordination environments were investigated using room-temperature Mössbauer spectroscopy. Glass transition temperatures (Tg) were determined via both differential scanning calorimetry (DSC) and dilatometry, following controlled heating–cooling cycles. At 1600 °C, the oxygen fugacity corresponds approximately to 2.4 log units above the quartz–fayalite–magnetite (QFM) buffer [37]. The base composition (NAS 1) was loaded with varying FeO_{tot} content (2.2–8.2 wt %), replacing SiO_2 while keeping Al_2O_3 and Na_2O nearly constant. The Fe^{3+}/Fe_{tot} ratio ranges from 0.60 to 0.75. Density increases (2.408–2.603 g/cm^3), while T_g decreases (478.7–466.2 °C) with iron content to increase at 477.9 °C when FeO_{tot} content reaches 13.9 wt%. The atomic packing density (C_g) remains nearly stable. See details in Table 1.

For structural characterization, Raman spectroscopy was performed in the spectral range from 200 to 1300 cm^{-1} by using a Thermo Scientific DXR2 spectrometer. Unpolarized Raman spectra were excited by means of a switchable solid-state laser ($\lambda_{exc} = 532$ nm) and an edge filter was used to cut off the Rayleigh line. The scattered radiation was dispersed using a high-resolution grating (1800 grooves/mm) and detected by a thermo-electrically cooled charge-coupled device, achieving an average spectral resolution of 2.9 cm^{-1}.

Optical UV–Vis absorption on the powder material was collected using an Agilent Cary 5000 UV–Vis–NIR spectrophotometer coupled with an internal Diffuse Reflectance Accessory.

Photoluminescence (PL) excitation, emission and time-resolved spectroscopy was obtained by a Horiba-Jobin Yvon Fluorolog-3-2iHR320 instrument. For steady state PL measurements, a continuous CW xenon lamp was used as excitation source, and the signal was acquired in the visible region by an R928-PMT. For time-resolved PL measurements, a pulsed microsecond xenon lamp was used, and the signal was acquired in multi-channel-scaler (MCS) modality.

Table 1
Chemical composition (wt.%), Fe^{3+}/Fe_{tot} molar index, room-temperature density (ρ), atomic packing density (C_g), and glass transition temperatures (T_g) from dilatometry and DSC (10 °C/min), taken from Ref. [31].

	NAS 1	NASF 2	NASF 3	NASF 4	NASF 5	NASF 6
SiO_2	76.6	73.8	72.0	71.0	68.2	66.3
Al_2O_3	3.2	3.2	3.2	3.3	3.2	2.7
$FeO_{tot.}$	–	2.2	4.4	6.4	8.2	13.9
Na_2O	19.6	19.7	19.1	19.0	19.0	16.9
Fe^{3+}/Fe_{tot}	–	0.60	0.68	0.65	0.75	0.77
ρ [g cm^{-3}]	2.408	2.453	2.468	2.503	2.524	2.603
C_g	0.488	0.491	0.491	0.492	0.493	0.498
T_g [°C]	478.7	472.1	472.1	470.1	466.2	477.9

3. Results and discussion

The full Raman spectra of all NASF glasses, normalized to the intensity of the band centered at about 500 cm^{-1}, are shown in Fig. 1. The low-frequency spectra between 250 and 650 cm^{-1} consists of characteristic vibrational bands, and can be divided in three subsets. The first part (250–500 cm^{-1}) is dominated by vibrations of 5- and 6-membered rings, as well as chain-like rings. The second region (500–550 cm^{-1}) is primarily influenced by 4-membered rings (D_1 band), while the third subset around 600 cm^{-1} corresponds to 3-membered rings (D_2 band).

As the FeO_{tot} content increases, the R band (below 500 cm^{-1}) start to develop a noticeable shoulder from 4.4 wt% (NASF 3), indicating the formation of larger rings [38], while the D_1 band appears increasingly hybridized with the R_c band of binary Na_2O–SiO_2 systems, shifting toward higher frequencies and becoming more defined. This band (R_c) is associated with more ordered substructures, predominantly composed of small rings that may form either chains or larger configurations made up of interconnected small rings. These correspond to localized vibrational modes, such as defect structures that are vibrationally isolated or three-membered ring configurations. The disappearance of this band with increasing iron mimics a sort of crowding effect with the formation of more compact and dense units. The D_2 band, typically around 600 cm^{-1}, is not distinctly evident in this system. It appears as a shoulder in NAS 1 but gradually diminishes and nearly disappears in NASF 6, which contains 13.9 wt% FeO_{tot}.

The high-wavenumber (850–1250 cm^{-1}) region of Raman spectra of NASF glasses, likewise all silicate glasses, consists of a set of spectral components corresponding to different silica tetrahedral units (T), referred to as Q^n species, where n represents the number of bridging oxygens (BOs). These species, Q^1 (1 BO), Q^2 (2 BOs), Q^3 (3 BOs), and Q^4

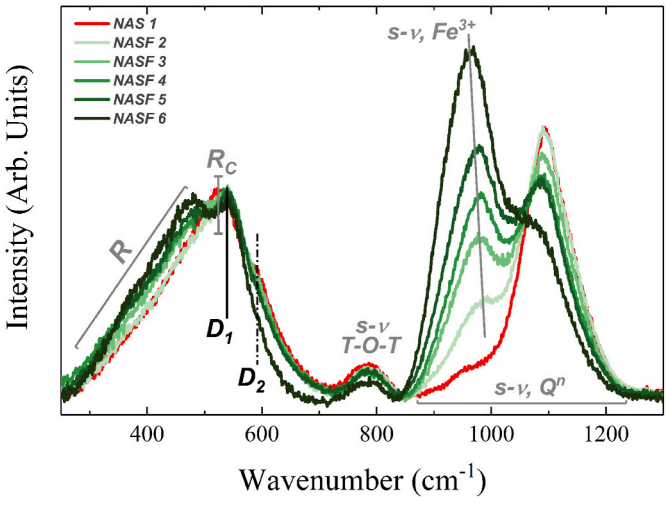

Fig. 1. Full Raman spectra of peralkaline iron-bearing soda aluminosilicate glasses.

(4 BOs), manifest as Gaussian-shaped bands centered at approximately 950, 990, 1090, and 1150 cm^{-1}, respectively. The broad spectral feature in this region results from the stretching vibrations of T–O bonds, influenced by variations in intertetrahedral bond angles, force constants, and T–O distances [39]. The distribution of these species in glasses is dictated by their composition, particularly the role of network modifiers (NM) and charge-balancing cations. In this system the Q^1 unit is not predicted while the component at ~1070 cm^{-1} Raman peak in the spectra of silica, silicate, and aluminosilicate glasses as corresponding to the stretching T^{2s} vibrational mode of TO_4 tetrahedra. In this mode, two oxygen atoms move closer to the central Si atom, while the other two oxygen atoms move away [40]. Therefore, the T^{2s} band is not related to a specific element, but rather to the local environment of bridging oxygens [41].

The spectra were deconvoluted to extract peak positions (cm^{-1}), areas (A), and full width at half maximum (FWHM), by constraining position to varies within 20 cm^{-1} respect to the initial peak position assigned value. The procedure used is analogous to that of Ref. [42,43] and results are reported in Fig. 2.

NAS 1, the iron-free glass, exhibits a moderately polymerized network dominated by Q^3 species (33.6 % area), indicative of an intermediate polymerization state. $Q^{4,II}$ (26.5 %) and $Q^{4,I}$ (9.3 %) suggest a substantial fraction of fully polymerized tetrahedra, while Q^2 (7.1 %) reflects a limited presence of depolymerized units, which is in line with the results in Ref. [31]. Upon iron incorporation, the glass structure undergoes progressive depolymerization, with an increase in Q^2 and a corresponding decrease in Q^3 and Q^4 species, signifying a breakdown of highly polymerized structures. The Fe^{3+} band intensifies with increasing iron content, confirming its strong Raman activity.

The increase in Q^2 is attributed to the formation of additional non-bridging oxygens (NBOs), reducing network connectivity. This feature is primarily produced by the effect of Na^+, however, the addition of six-fold coordinated Fe^{2+} and Fe^{3+} ($^{VI}Fe^{2+}$ and $^{VI}Fe^{3+}$) influences the glass network through charge disruption of bridging oxygens (BOs), competing with Na^+ for modifying the Al–Si framework.

At medium concentrations of $FeO_{tot.}$ (NASF 2, NASF 3, and NASF 4), $^{VI}Fe^{2+}$ and $^{VI}Fe^{3+}$ act as network modifiers, as indicated by the increased Q^2 and in part by Fe^{3+} component, further promoting depolymerization by increasing NBOs. For example, in NASF 2, the Q^2 (9.4 %) and Fe^{3+} bands (8.6 %) are present at 970.7 cm^{-1}, and similar trends are observed for NASF 3 and NASF 4 with corresponding increases in Q^2 and Fe^{3+} areas (17.9 % and 21.0 %, respectively), reflecting greater depolymerization.

At higher $FeO_{tot.}$ concentrations (NASF 5 and NASF 6), Fe^{3+} (and Fe^{2+}) likely substitutes for Si^{4+} or Al^{3+} in tetrahedral coordination ($^{IV}Fe^{2+}$ and $^{IV}Fe^{3+}$), as demonstrated by Mössbauer data in Ref. [8]. In NASF 5, for instance, the Fe^{3+} band is prominent with a significant intensity of 30.2 % at 978.8 cm^{-1}, while the Q^2 (16.7 %) and T^{2s} (25.3 %) peaks remain noticeable, further suggesting a network-modifying role of iron in these compositions. Worth of note, is that Q^2 area drops to 8.7 % in NASF 6 (value comparable to the iron-free NAS 1 glass) and it suggests a structural reorganization in favor of more BOs thus, a more polymerized network.

Similarly, the Q^3 unit may encompass contributions from $^{IV}Fe^{3+}$ (in a fourfold coordination state), introducing an additional component at approximately 970 cm^{-1}.

As the iron content increases, the Q^3 area decreases, reflecting an apparent decrease of the network connectivity and the formation of (NBOs). However, the reduction in the Q^3 units becomes more pronounced with increasing iron content, particularly in NASF 6, where Fe^{3+} partially replaces network-forming cations like Al^{3+} and Si^{4+}, leading to the formation of BOs instead of NBOs and contributing to the network polymerization as suggested by Mössbauer data [31].

For instance, the peak at 970.7 cm^{-1} in NASF 2 and 969.5 cm^{-1} in NASF 3 supports this hypothesis, although these secondary effects are overlooked in this analysis, as the high-wavenumber spectral profiles remain largely consistent across samples.

The observed band-splitting of Q^4 species, occurring between 1080 and 1200 cm^{-1}, is attributed to variations in the T–O–T bond angle, influenced by coexisting Al–O–Si and Si–O–Si linkages. In Table 2, the $Q^{4,I}$ and $Q^{4,II}$ bands for NAS 1, NASF 2, and NASF 3 (ranging between 1138 and 1170 cm^{-1}) does not show consistent frequency shift, but their areas decrease as the iron content increases, signaling a breakdown of the highly polymerized network and an increase in depolymerization. This decrease is more pronounced for $Q^{4,I}$ than for $Q^{4,II}$, especially in higher iron concentrations (NASF 5 and NASF 6), reflecting the

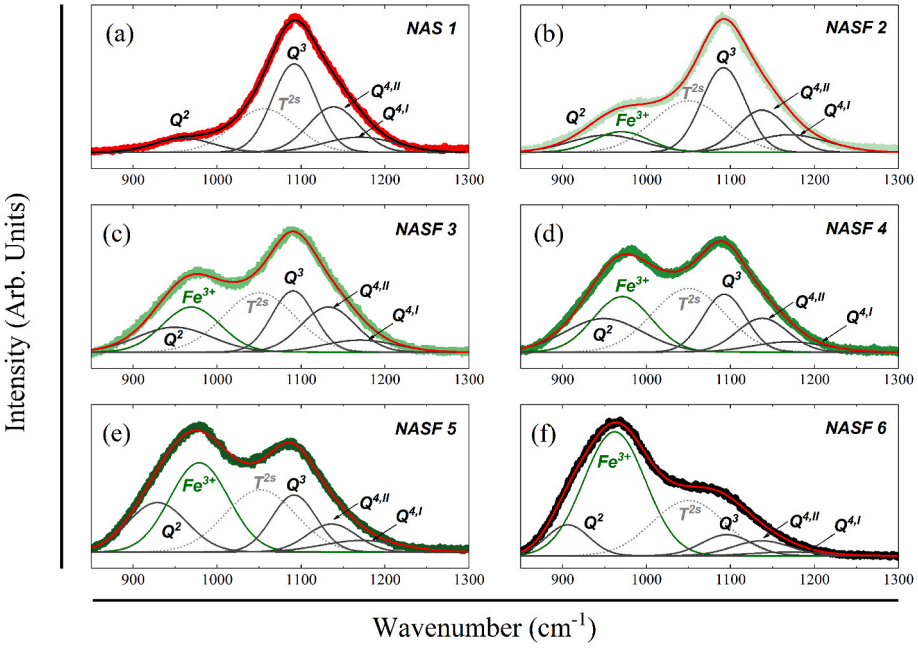

Fig. 2. Deconvolution of the stretching region in the Raman spectral window between 850 and 1300 cm^{-1}, where the cumulative fitting curves are depicted in orange, while the individual Gaussian components are represented by the different lines. (For interpretation of the references to color in this figure legend, the reader is referred to the Web version of this article.)

Table 2
Deconvolution data. Band position (ω in cm^{-1}), error is < 4 cm^{-1}; % band area (A), the relative error is <5 %) and the full width at half maximum (FWHM in cm^{-1}), error <7 cm^{-1}.

Sample	Unit	ω (cm^{-1})	A (%)	FWHM (cm^{-1})
NAS 1	Q^2	960.8	7.1	82.4
	T^{2s}	1056.0	23.6	88.8
	Q^3	1071.9	33.6	61.8
	$Q^{4,II}$	1138.7	26.5	70.6
	$Q^{4,I}$	1170.0	9.3	100.1
NASF 2	Q^2	951.9	9.4	101.5
	Fe^{3+}	970.7	8.6	77.4
	T^{2s}	1050.8	27.9	100.1
	Q^3	1099.7	28.1	61.3
	$Q^{4,II}$	1137.4	15.9	69.9
	$Q^{4,I}$	1170.3	10.0	106.3
NASF 3	Q^2	949.2	12.7	104.6
	Fe^{3+}	969.5	17.9	81.2
	T^{2s}	1050.0	29.0	100.1
	Q^3	1090.5	17.8	59.6
	$Q^{4,II}$	1132.6	16.8	76.3
	$Q^{4,I}$	1170.3	5.9	100.1
NASF 4	Q^2	949.1	16.9	108.9
	Fe^{3+}	971.0	21.0	81.6
	T^{2s}	1050.0	30.0	101.5
	Q^3	1092.6	16.1	60.0
	$Q^{4,II}$	1137.9	11.2	71.2
	$Q^{4,I}$	1170.0	4.8	101.6
NASF 5	Q^2	928.9	16.7	82.4
	Fe^{3+}	978.8	30.2	82.4
	T^{2s}	1052.0	25.3	98.9
	Q^3	11092.6	14.6	62.6
	$Q^{4,II}$	1136.5	8.0	69.4
	$Q^{4,I}$	1171.8	5.1	109.5
NASF 6	Q^2	906.2	8.7	59.5
	Fe^{3+}	961.9	50.6	86.4
	T^{2s}	1049.8	26.4	100.9
	Q^3	1095.7	6.9	70.1
	$Q^{4,II}$	1137.1	5.7	80.6
	$Q^{4,I}$	1170.4	1.8	101.6

structural modification induced by iron, particularly Fe^{3+} and Fe^{2+} ions which is not related to depolymerization for this compositional threshold (occurring at about 8.2 wt% of FeO_{tot}).

The FWHM values of $Q^{4,I}$ and Fe^{3+} bands increase with iron content, indicating greater structural disorder. In NASF 5 and NASF 6, the FWHM values for the $Q^{4,I}$ band (100.1 cm^{-1} and 101.6 cm^{-1}, respectively) and the Fe^{3+} band (82.4 cm^{-1} and 86.4 cm^{-1}, respectively) are significantly larger compared to NAS 1 (82.4 cm^{-1}) and NASF 2 (77.4 cm^{-1}). This suggests that the incorporation of iron leads to increased structural disorder. Following, density increase from NAS 1 to NASF 6 reflects both atomic weight and structural rearrangement, while the ~4 % rise in C_g suggests a modest gain in network connectivity. Iron influences this balance: tetrahedrally coordinated Fe enhances bond strength and rigidity, whereas Fe^{2+} as a modifier increases structural mobility and rearrangement near T_g, leading to higher fragility [44,45].

This progressive Fe-enrichment trend corresponds to a decrease in viscosity and an increase in fragility, which could impact the melting behavior and mechanical properties of the glasses. In particular, the increased FWHM values for NASF 5 and NASF 6 reflect this disorder, potentially influencing the glasses' fragility and mechanical strength [46].

The diffuse reflectance of the samples is reported in Fig. 3 (left). The addition of Fe is responsible for a strong increase in the absorbance, and a shift of the absorption edge to the higher wavelengths, as revealed also by the browning of the sample color. In agreement with previous observations, upon Fe incorporation, the glass structure undergoes progressive depolymerization, with the formation of additional non-bridging oxygens (NBOs) that reduce network connectivity. Since NBOs have higher energy than the bonded orbitals, their increase leads to an increase of the valence band energy and a decrease of the forbidden bandgap energy [47,48]. This results in a higher absorption of UV photons and a shift to lower energies (higher wavelength) of the absorption edge. Moreover, additional peaks can be observed in the Fe containing samples, unlike the one without Fe. These peaks correspond to transitions within the energy level diagram of Fe^{3+} ions in a host lattice, reported in Fig. 3 (right) [49]. The exact energy level positions depend on the host lattice and from the local symmetry surrounding Fe^{3+} ions [50,51]. In particular, the scheme reports the transitions responsible for the observed peaks in the spectra: $^6A_1(S) \rightarrow {}^4E(D)$ at 3.28 eV (378 nm), $^6A_1(S) \rightarrow {}^4T_2(D)$ at 2.96 eV (419 nm), $^6A_1(S) \rightarrow {}^4A_1{}^4E(G)$ at 2.75 eV (450 nm). The photoluminescence (PL) emission of photons at about 1.78 eV (700 nm) is also shown, but it will be discussed later.

The equivalent α can be calculated from diffuse reflectance spectra by using the Kubelka-Munk Eq. (1) for samples with high scattering and low transmission like powder samples.

$$F(R_\infty) = \frac{K}{S} = \frac{(1-R_\infty)^2}{2R_\infty} \quad (1)$$

where $F(R_\infty)$ is the Kubelka-Munk function, which is equivalent to α, R_∞ is the reflectance of an infinitely thick specimen, while K and S are the

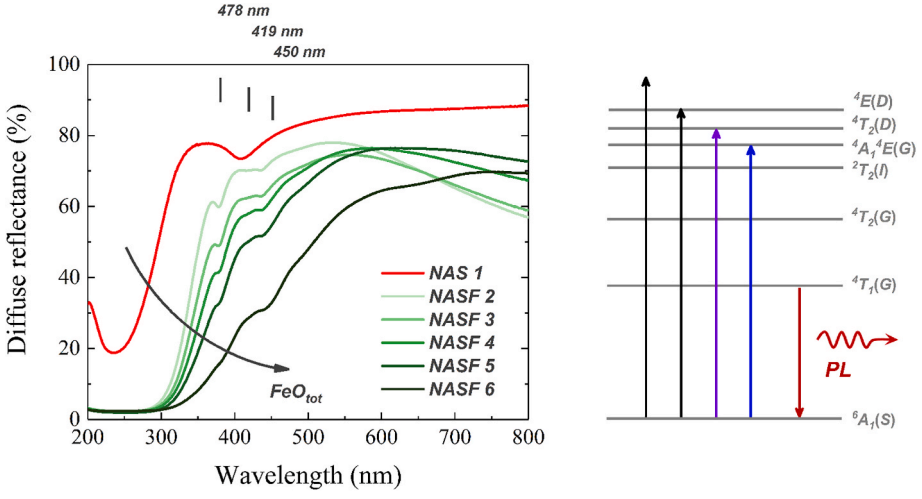

Fig. 3. Diffuse reflectance (%) of the soda aluminosilicate glass powders with different Fe contents (left) and schematic energy-level diagram of Fe^{3+} in a host lattice (right).

Kubelka-Munk absorption and scattering coefficients.

A deeper understanding of the effect of Fe doping on the optical properties of the glass was obtained by Tauc plot calculation of the optical energy gap and by evaluating the Urbach energy of the material, as shown in Fig. 4. The energy gap E_g is the energy separation between the top of the valence band and the bottom of the conduction band. The Tauc method for calculating E_g is based on the assumption that the energy-dependent absorption coefficient α, or equivalently $F(R_\infty)$ for powders, can be expressed by the following equation [52]:

$$(\alpha \cdot h\nu)^{1/\gamma} = B(h\nu - E_g) \tag{2}$$

where h is the Planck constant, ν is the photon's frequency, E_g is the band gap energy, and B is a constant. The γ factor depends on the nature of the electron transition and is equal to 1/2, 2, 3/2 and 3 for the direct allowed, indirect allowed, direct forbidden and indirect forbidden transition, respectively [53]. In this work, the value of n is considered to be 2 to calculate the indirect allowed transition which usually takes place in glasses. By extrapolating the linear part of the curve (higher $h\nu$ region) to the x-axis (dashed line), it is possible to obtain Eg as the intercept on the x-axis, as shown in Fig. 4 (a).

It should be noted that this approach should be applied only if materials do not absorb light below the bandgap energy. When a considerable absorbance occurs at energies below E_g, the obtained results may be significantly underestimated. This usually happens for defected, doped or surface modified materials where intra-band states reflect in the absorption spectrum as an Urbach tail, i.e., an additional broad absorption band, which should be considered to determine the correct bandgap energy, as reported by Makula et al. in Ref. [54]. In such cases, those authors demonstrated that a direct application of the Tauc method results in an inaccurate underestimation of E_g, although it appears frequently in several publications. A simple way to account for it is adding a linear fit below the fundamental absorption and considering the intersection of the two fitting lines. This approach is also reported in Fig. 4 (a). The values of E_g obtained by the two approaches (as the intercept with the axis and corrected for the Urbach tail) are reported in Fig. 4 (c), showing that for our samples the highest difference occurs in NASF 6, which has the highest Fe concentration.

As a further analysis, a quantification of the Urbach tail can be obtained by calculating the Urbach energy E_U, which is related to the defect or disorder degree in the system [55,56]. The Urbach energy quantifies the steepness of the onset of absorption near the band edge, and hence the broadness of the density of states: a sharper onset of absorption represents a lower Urbach Energy. E_U can be obtained by the following equation:

$$\alpha = \alpha_0 \exp\left(\frac{h\nu - E_g}{E_U}\right) \implies \ln \alpha = \frac{1}{E_U} h\nu + C \tag{4}$$

where α_0 is a constant which is called tailing parameter and C is a constant. With a few simple passages, it is possible to show that $\ln \alpha$ is proportional to $h\nu$. The value of E_U can be obtained by the slope of the curve in the linear region corresponding to the higher photon energies, as shown in Fig. 4 (b). The obtained E_U values are reported in Fig. 4 (c). With the increase of Fe content, E_U decreases first and then increases. On the other hand, the decrease of Eg is mainly due to the fact that addition of Fe reduces the average bond energies of the whole glass system [57].

A deeper explanation of these behaviors can be obtained considering the role of Fe within these glasses. The investigated compositions are characterized by an increase of the network modifiers $^{VI}Fe^{2+}$ and $^{VI}Fe^{3+}$ ions (as shown by Mössbauer data in Ref. [31]) that disrupt the polymerized structure of the glass. This effect is consistent up to a concentration of 6.4 wt% of FeO_{tot}, while from 8.4 wt% a self-compensation process of the charges through a re-enrichment of tetrahedral units occurs. Indeed, NASF 5 and 6 show tetrahedral units in both Fe^{2+} and Fe^{3+}. This increasing iron load creates additional defects between the conduction and the valence bands that are probably caused by the modifiers $^{VI}Fe^{2+}$ and $^{VI}Fe^{3+}$. These defects result in the formation of more dangling bonds and non-bridging oxygens (NBO), ultimately narrowing the bandgap by reducing the energy separation between the valence band maximum and the conduction band minimum [47], as confirmed by the red-shift of the cut-off wavelength in the absorption spectrum shown in

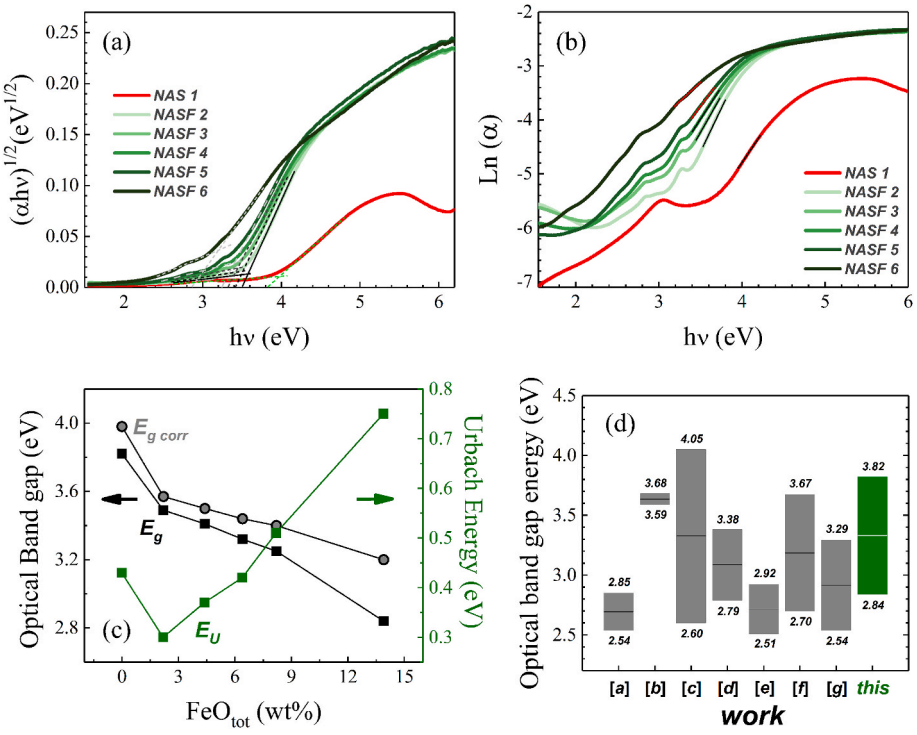

Fig. 4. (a) Tauc plot for optical bandgap E_g calculation. (b) Urbach energy E_U calculation. (c) Plot of bandgap and Urbach energy as a function of FeO_{tot}. (d) Comparison of E_g for different glass systems [a] = [58], [b] = [59], [c] = [60], [d] = [61], [e] = [62], [f] = [63], [g] = [48].

Fig. 3. Moreover, the coordination defects induced by Fe (dangling bonds) and the increasing free oxygen will reduce the width of the forbidden band, which will help to develop the application of Fe-doped NASF glasses in semiconductor materials. Also, E_U represents an indication of structural disorder. Generally speaking, the bigger E_U reflects lower structural stability. The initial decrease in E_U value demonstrates that the presence of Q^3 and Q^4 units promotes the continuity of the silica network, thereby ensuring structural stability by Fe addition to NAS 1 glass. As the effect of network-modifying ions introduction ($^{VI}Fe^{2+}$ and $^{VI}Fe^{3+}$), the number of NBOs rises, leading to greater depolymerization of the silica network which reflects in higher disorder. Moreover, the increase of FeO_{tot} is also related to glass densification, as attested by the atomic packing density. This densification leads to a reduction in the optical bandgap and a rise in the E_U value, attributed to changes in the bonding state within the FeO_{tot}-loaded NASF glass system, where an increasing atomic packing fraction and density correspond to a growing molar volume from NAS to NASF 6 [31].

Fig. 4 (d) presents the comparison of *Eg* values for different Fe-doped glass systems. Due to comparison purposes with other literature papers, the value of *Eg* that is reported was the one calculated by standard Tauc analysis [48,58–63]. As a general comment, according to the literature, the *Eg* of the different glass systems decrease after Fe doping in a range which depends on the glass composition and doping content.

The PL excitation and emission spectra of the samples are reported in Fig. 5. It is worth observing a significant PL intensity for the reference NAS 1 undoped glass, with a broad emission made of a main peak centered around 525 nm and a secondary lobe around 675 nm. Luminescence from Al_2O_3 containing glasses under UV excitation was already reported in the literature [64–66]. Similar bands around 500–550 nm and 650–700 nm were observed. The green band has been attributed to alanol and silanol-related centers, such as Al–OH and Si–OH chemical bonds. The red band was instead attributed to non-bridging oxygen hole centers (NBOHCs). A detailed discussion of the PL properties of these luminescent centers is reported in Ref. [65].

After the introduction of Fe in the matrix, a significant drop of intensity is observed, and the fingerprint of Fe^{3+} optical transitions clearly emerges in the PLE of Fig. 5 (left), as previously discussed in the diffuse reflectance spectra, in particular $^6A_1(S)\rightarrow{}^4E(D)$ at 3.28 eV (378 nm), $^6A_1(S)\rightarrow{}^4T_2(D)$ at 2.96 eV (419 nm), $^6A_1(S)\rightarrow{}^4A_1{}^4E(G)$ at 2.75 eV (450 nm). This observation is further corroborated by the PL emission spectra in Fig. 5 (right), showing a broad emission peaked around 700 nm, corresponding to the $^4T_1(G) \rightarrow {}^6A_1(S)$ transition at 1.78 eV. The PL intensity decreases with increasing iron content, in relation to the increase of defectivity of the matrix, as observed previously, which introduces additional energy levels within the bandgap and therefore non-radiative recombination paths. Moreover, it was reported in the literature that Fe^{3+} clustering occurs in silicate glasses even at low concentrations [36], which results in a significant quenching of the emission.

Fig. 6 reports time resolved PL decay curves and lifetime analysis for the different samples. In Fig. 6 (a) the PL decay of NAS 1 is reported for 530 nm and 680 nm emission, showing a predominant fast recombination, of the order of microseconds, followed by a longer tail, in particular for the red emission component, which agrees with the literature data and behavior reported for –OH and NBO centers [65]. A completely different shape can be observed in Fig. 6 (b) for the Fe doped samples, which can be described by the contribution of several exponential decays. By increasing of the Fe content the lifetime significantly decreases, in agreement with the increase of disorder in the matrix, clustering of Fe^{3+} and the addition of non-radiative recombination paths.

Lifetime elaboration was performed by using a triple exponential decay, as shown in the example reported in Fig. 6 (c) for NASF 4 glass. Due to the strong correlations between the fitting parameters, a triple exponential is unusual for lifetime decay fitting, but in our samples this approach is justified to account for the three different contributions which are responsible for the red emission. The first component is due to fast recombinations, even shorter than the pulsed excitation lamp. Therefore, the lifetime of this component was fixed for all the samples at 1 μs after testing different possibilities. Fixing the fast component lifetime significantly reduces correlations and guarantees more reliability in the other two components. The second and third components, whose lifetimes are reported in Fig. 6 (d), are related to the matrix, possibly NBO centers, and to the Fe^{3+} emission. It is worth observing that the lifetime obtained for the matrix is almost the same for all the samples, around 150–200 μs, while the emission from Fe^{3+} follows a significant decrease from 1.7 ms to 0.22 ms, as a consequence of the previously discussed quenching mechanisms.

Worth note, this study highlights how correlation between optical, compositional and structural properties, is relevant both for geological processes (*i.e.* volcanic eruptions), geomaterials and industrial processing. Understanding these effects is crucial for better interpreting the physics behind the iron-bearing glass systems.

4. Conclusions

The influence of iron on the structural and optical properties of peralkaline soda aluminosilicate glasses (NASF) has been investigated. It was shown that Fe doping significantly affects the glass network, altering both its structural connectivity and optical properties. Iron incorporation progressively depolymerizes the network. At moderate FeO_{tot} concentrations, Fe^{2+} and Fe^{3+} act as network modifiers, increasing the number of non-bridging oxygens (NBOs). At high iron concentrations, they replace Si^{4+} and Al^{3+} in tetrahedral coordination, promoting network repolymerization. Increasing iron induces structural disorder and the formation of clustering, increasing optical absorption and reducing the bandgap, as attested by Tauc plot and Urbach energy calculations. The presence of Fe^{3+} ions is revealed also by photoluminescence absorption and emission, showing the characteristic optical transitions. PL intensity and lifetime decrease with iron content,

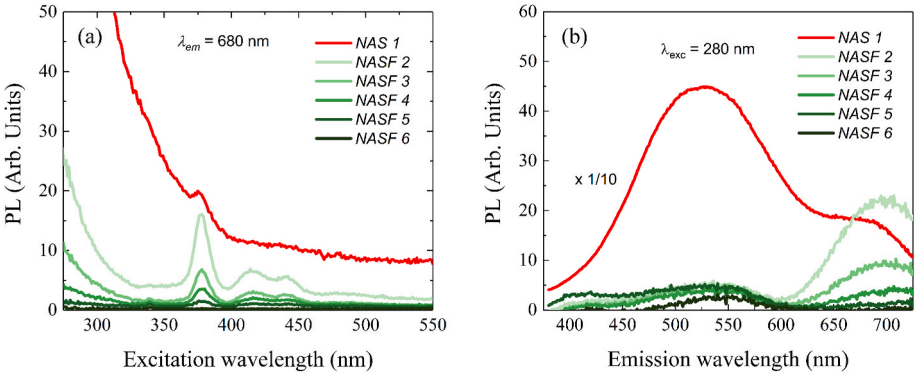

Fig. 5. PL excitation spectra (left) and emission spectra (right) for the different samples with increasing Fe content.

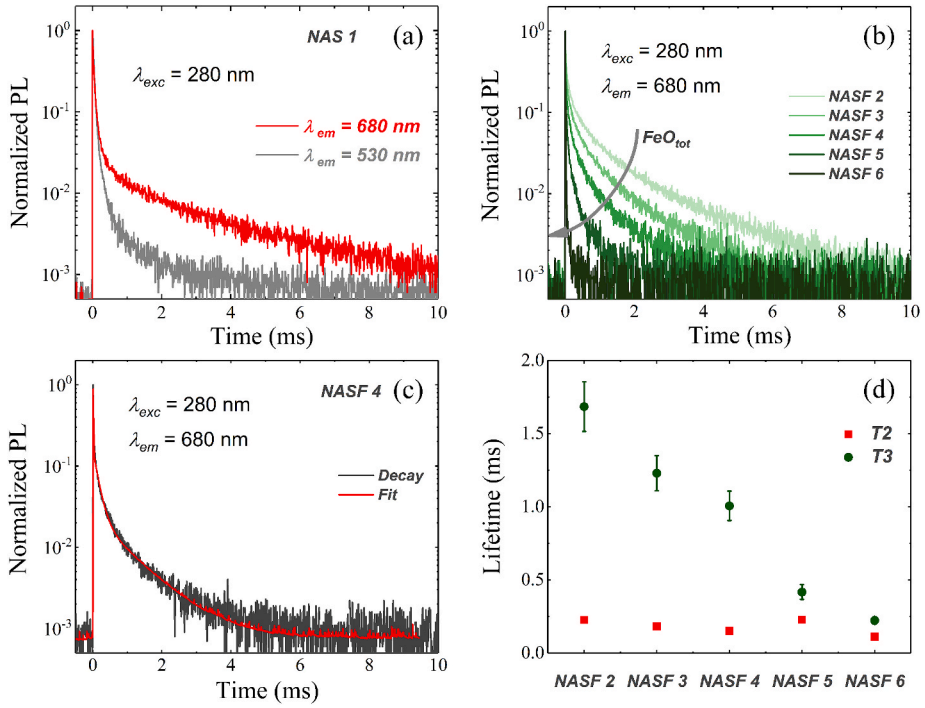

Fig. 6. Time resolved PL emission and lifetime elaboration data for the different samples with increasing Fe content. (a) Normalized PL decay of NAS 1 under 280 nm excitation and 530 nm, 680 nm emission. (b) Normalized PL decay of Fe doped samples under 280 nm excitation and 680 nm emission. (c) Example of the fitting procedure for NASF 4 sample. (d) Exponential decay lifetimes T2 and T3 obtained from the long tail fitting.

confirming an increase in non-radiative recombination pathways and quenching mechanisms related to defects and iron clustering.

CRediT authorship contribution statement

Michele Cassetta: Writing – review & editing, Writing – original draft, Methodology, Investigation, Formal analysis, Data curation, Conceptualization. **Anna Safonova:** Writing – review & editing, Investigation, Formal analysis, Data curation. **Gino Mariotto:** Writing – review & editing, Validation, Methodology, Investigation, Data curation. **Nicola Daldosso:** Writing – review & editing, Supervision, Resources, Investigation, Funding acquisition. **Shujie You:** Investigation, Formal analysis, Data curation. **Pawan Kumar:** Investigation, Data curation. **Alberto Vomiero:** Writing – review & editing, Supervision, Investigation. **Mohamed Yousri Ben Zaied:** Investigation, Formal analysis, Data curation. **Mongi Bouaicha:** Validation. **Francesco Enrichi:** Writing – review & editing, Writing – original draft, Supervision, Methodology, Investigation, Funding acquisition, Formal analysis, Data curation, Conceptualization.

Declaration of competing interest

The authors declare that they have no known competing financial interests or personal relationships that could have appeared to influence the work reported in this paper.

Acknowledgements

All the authors acknowledge Dr. Marco Giarola of Centro Piattaforme Tecnologiche (CPT) of the University of Verona for technical support with the use of instruments and Dr. Daniele Giordano, Dr. Sonia La Felice, Prof. Mattia Biesuz and Prof. Vincenzo Sglavo for support, resources and glass synthesis.

F.E. and N.D. acknowledge RiBa 2022 internal projects of University of Verona and M.Y.B.Z. the MoCoSvi - Mobilità per la Cooperazione allo Sviluppo Internazionale grant of the Universiy of Verona.

M.C. acknowledges support from PNRR M4C2 - PRIN 2022PXHTXM - STONE – "A new generation Spectroscopy Tool to monitor rheology and phase transformation prOcesses in volcaNology and cEramic production" funded by the European Union.

Data availability

Data will be made available on request.

References

[1] H. Yamazaki, S. Yamamoto, Glass for lighting, Encycl. Glass Sci. Technol. Hist. Cult. (2021) 775–785, https://doi.org/10.1002/9781118801017.CH6.9.

[2] F. Enrichi, G. Mastantuoni, M. Cassetta, A. Sambugaro, N. Daldosso, A. Martucci, A. Vomiero, E. Cattaruzza, G.C. Righini, Structural and optical properties of Eu3+-doped sol–gel silica–soda glasses, Eur. Phys. J. Plus 139 (2024) 346, https://doi.org/10.1140/EPJP/S13360-024-05151-W.

[3] D. Ehrt, W. Seeber, Glass for high performance optics and laser technology, J. Non-Cryst. Solids 129 (1991) 19–30, https://doi.org/10.1016/0022-3093(91)90076-I.

[4] J. Ballato, P. Dragic, Rethinking optical fiber: new demands, old glasses, J. Am. Ceram. Soc. 96 (2013) 2675–2692, https://doi.org/10.1111/JACE.12516;PAGEGROUP:STRING:PUBLICATION.

[5] A. Martucci, M. De Nuntis, A. Ribaudo, M. Guglielmi, S. Padovani, F. Enrichi, G. Mattei, P. Mazzoldi, C. Sada, E. Trave, G. Battaglin, F. Gonella, E. Borsella, M. Falconieri, M. Patrini, J. Fick, Silver-sensitized erbium-doped ion-exchanged sol-gel waveguides, Appl. Phys. A Mater. Sci. Process. 80 (2005) 557–563, https://doi.org/10.1007/s00339-004-2967-5.

[6] F. Enrichi, C. Armellini, G. Battaglin, F. Belluomo, S. Belmokhtar, A. Bouajaj, E. Cattaruzza, M. Ferrari, F. Gonella, A. Lukowiak, M. Mardegan, S. Polizzi, E. Pontoglio, G.C. Righini, C. Sada, E. Trave, L. Zur, Silver doping of silica-hafnia waveguides containing Tb3+/Yb3+ rare earths for downconversion in PV solar cells, Opt. Mater. 60 (2016) 264–269, https://doi.org/10.1016/j.optmat.2016.07.048.

[7] F. Enrichi, G. Mattei, C. Sada, E. Trave, D. Pacific, G. Franzò, F. Priolo, F. Iacona, M. Prassas, M. Falconieri, E. Borsella, Evidence of energy transfer in an aluminosilicate glass codoped with Si nanoaggregates and Er3+ ions, J. Appl. Phys. 96 (2004) 3925, https://doi.org/10.1063/1.1776637.

[8] J. Yu, M. Luo, Z. Lv, S. Huang, H.H. Hsu, C.C. Kuo, S.T. Han, Y. Zhou, Recent advances in optical and optoelectronic data storage based on luminescent nanomaterials, Nanoscale 12 (2020) 23391–23423, https://doi.org/10.1039/D0NR06719A.

[9] Z. Chai, X. Hu, F. Wang, X. Niu, J. Xie, Q. Gong, Ultrafast all-optical switching, Adv. Opt. Mater. 5 (2017) 1600665, https://doi.org/10.1002/ADOM.201600665.

[10] D. Manzani, J.B. Souza Junior, A.S. Reyna, M.L. Silva Neto, J.E.Q. Bautista, S.J. L. Ribeiro, C.B. De Araújo, Phosphotellurite glass and glass-ceramics with high TeO2 contents: thermal, structural and optical properties, Dalton Trans. 48 (2019) 6261–6272, https://doi.org/10.1039/C9DT00691E.

[11] D. Li, X. Zheng, H. He, P. Boutinaud, S. Xiao, J. Xu, C. Wang, Y. Hu, F. Kang, A 20-Year review of inorganic photochromic materials: design consideration, synthesis methods, classifications, optical properties, mechanism models, and emerging applications, Laser Photon. Rev. 18 (2024) 2400742, https://doi.org/10.1002/LPOR.202400742;JOURNAL:JOURNAL:18638899;WGROUP:STRING:PUBLICATION.

[12] J.F. Schroeder, N.F. Borelli, Tribute to photosensitive glasses [invited], Opt. Mater. Express 12 (9) (2022) 3480–3492, https://doi.org/10.1364/OME.459279, 3480-3492 12.

[13] C. Rizal, H. Shimizu, J.R. Mejía-Salazar, Magneto-optics effects: new trends and future prospects for technological developments, Magnetochemistry 8 (2022) 94, https://doi.org/10.3390/MAGNETOCHEMISTRY8090094, 94 8 (2022).

[14] R. Mazzaro, A. Vomiero, The Renaissance of luminescent solar concentrators: the role of inorganic nanomaterials, Adv. Energy Mater. 8 (2018) 1801903, https://doi.org/10.1002/AENM.201801903;PAGEGROUP:STRING:PUBLICATION.

[15] A. Chiappini, L. Zur, F. Enrichi, B. Boulard, A. Lukowiak, G.C. Righini, M. Ferrari, Glass ceramics for frequency conversion, in: F. Enrichi, G.C. Righini (Eds.), Solar Cells and Light Management: Materials, Strategies and Sustainability, Elsevier, 2019.

[16] T. Gatti, F. Lamberti, R. Mazzaro, I. Kriegel, D. Schlettwein, F. Enrichi, N. Lago, E. Di Maria, G. Meneghesso, A. Vomiero, S. Gross, Opportunities from doping of non-critical metal oxides in last generation light-conversion devices, Adv. Energy Mater. 11 (2021) 2101041, https://doi.org/10.1002/AENM.202101041.

[17] L. Zur, C. Armellini, S. Belmokhtar, A. Bouajaj, E. Cattaruzza, A. Chiappini, F. Coccetti, M. Ferrari, F. Gonella, G.C. Righini, E. Trave, A. Vomiero, F. Enrichi, Comparison between glass and glass-ceramic silica-hafnia matrices on the down-conversion efficiency of Tb3+/Yb3+ rare Earth ions, Opt. Mater. 87 (2019) 102–106, https://doi.org/10.1016/j.optmat.2018.05.008.

[18] F. Enrichi, G.C. Righini (Eds.), Solar Cells and Light Management: Materials, Strategies and Sustainability, Elsevier, 2019.

[19] G.C. Righini, F. Enrichi, L. Zur, M. Ferrari, Rare-earth doped glasses and light managing in solar cells, J. Phys. Conf. Ser. 1221 (2019) 012028, https://doi.org/10.1088/1742-6596/1221/1/012028.

[20] E. Cattaruzza, V.M. Caselli, M. Mardegan, F. Gonella, G. Bottaro, A. Quaranta, G. Valotto, F. Enrichi, Ag+↔Na+ion exchanged silicate glasses for solar cells covering: down-Shifting properties, Ceram. Int. 41 (2015) 7221–7226, https://doi.org/10.1016/j.ceramint.2015.02.060.

[21] F. Enrichi, M. Cassetta, N. Daldosso, E. Cattaruzza, P. Riello, R. Zairov, A. Vomiero, G.C. Righini, Effect of the crystal structure on the optical properties and Ag sensitization of Tb3+/Yb3+ ions in silica-zirconia glasses and glass-ceramics, Ceram. Int. (2022), https://doi.org/10.1016/j.ceramint.2022.10.036.

[22] W. Blanc, Y. Gyu Choi, X. Zhang, M. Nalin, K.A. Richardson, G.C. Righini, M. Ferrari, A. Jha, J. Massera, S. Jiang, J. Ballato, L. Petit, The past, present and future of photonic glasses: a review in homage to the United Nations International Year of glass 2022, Prog. Mater. Sci. 134 (2023) 101084, https://doi.org/10.1016/j.pmatsci.2023.101084.

[23] H. Félix-Quintero, I. Camarillo-Garcìa, J. Hernández-Alcántara, E. Camarillo-García, A. Cordero-Borboa, C. Flores-Jiménez, M. García-Hipólito, F. Ramos-Brito, D. Acosta-Najarro, H. Murrieta-Sánchez, RGB emission of Mn2 + doped zinc phosphate glass, J. Non-Cryst. Solids 466–467 (2017) 58–63, https://doi.org/10.1016/j.jnoncrysol.2017.04.002.

[24] Q. Huang, T. Liu, X. Shen, X. Li, A. Lu, Y. Gu, Characterization of Fe2O3 doping on structure, optical and luminescence properties of magnesium aluminosilicate-based glasses, J. Non-Cryst. Solids 563 (2021), https://doi.org/10.1016/j.jnoncrysol.2021.120786.

[25] M.A. Marzouk, S.M. Abo-Naf, H.A. Zayed, N.S. Hassan, Photoluminescence and semiconducting behavior of Fe, Co, Ni and Cu implanted in heavy metal oxide glasses, J. Mater. Res. Technol. 5 (2016) 226–233, https://doi.org/10.1016/j.jmrt.2015.11.003.

[26] R.K. Chinnam, A.A. Francis, J. Will, E. Bernardo, A.R. Boccaccini, Review. Functional glasses and glass-ceramics derived from iron rich waste and combination of industrial residues, J. Non-Cryst. Solids 365 (2013) 63–74, https://doi.org/10.1016/j.jnoncrysol.2012.12.006.

[27] M. Wilke, Fe in magma - an overview, Ann. Geophys. 48 (2005) 609–617, https://doi.org/10.4401/ag-3222.

[28] C. Le Losq, M.R. Cicconi, D.R. Neuville, Iron in silicate glasses and melts: implications for volcanological processes, Magma Redox Geochem. (2021) 233–253, https://doi.org/10.1002/9781119473206.ch12.

[29] R. Antonio, J. Bussey, M.C.J.D. Wilkins, D. Neuville, L. Cormier, J. McCloy, Effects of Al substitution for Fe in Na 5 FeSi 4 O 12, Glass Europe 2 (2024) 151–164.

[30] M. Zimova, S. Webb, The effect of chlorine on the viscosity of Na2O-Fe2 O3-Al2O3-SiO2 melts, Am. Mineral. 91 (2006) 344–352, https://doi.org/10.2138/am.2006.1799.

[31] M. Cassetta, E. De Bona, A. Sambugaro, F. Enrichi, N. Daldosso, B. Giannetta, C. Zaccone, M. Biesuz, V.M. Sglavo, R. Almeev, L. Nodari, D. Giordano, G. Mariotto, Fe-dependent structural evolution of peralkaline soda aluminosilicate glasses: iron speciation vs. glass transition, Chem. Geol. 674 (2025) 122561, https://doi.org/10.1016/J.CHEMGEO.2024.122561.

[32] F. Di Fiore, A. Vona, A. Costa, S. Mollo, C. Romano, Quantifying the influence of cooling and shear rate on the disequilibrium rheology of a trachybasaltic melt from mt. Etna, Earth Planet Sci. Lett. 594 (2022) 117725, https://doi.org/10.1016/J.EPSL.2022.117725.

[33] A. Scarani, A. Zandonà, F. Di Fiore, P. Valdivia, R. Putra, N. Miyajima, H. Bornhöft, A. Vona, J. Deubener, C. Romano, D. Di Genova, A chemical threshold controls nanocrystallization and degassing behaviour in basalt magmas, Commun. Earth Environ. 3 (1) (2022) 1–14, https://doi.org/10.1038/s43247-022-00615-2, 2022 3.

[34] F. Di Fiore, A. Vona, D. Di Genova, A. Pontesilli, L. Calabrò, S. Mollo, J. Taddeucci, C. Romano, P. Scarlato, Magma titanium and iron contents dictate crystallization timescales and rheological behaviour in basaltic volcanic systems, Commun. Earth Environ. 5 (2024) 1–13, https://doi.org/10.1038/S43247-024-01452-1. SUBJMETA=2151,431,598,704;KWRD=PETROLOGY,VOLCANOLOGY.

[35] P.A. Bingham, J.M. Parker, T. Searle, J.M. Williams, I. Smith, Novel structural behaviour of iron in alkali-alkaline-earth-silica glasses, C. R. Chim. 5 (2002) 787–796, https://doi.org/10.1016/S1631-0748(02)01444-3.

[36] P.A. Bingham, J.M. Parker, T. Searle, J.M. Williams, K. Fyles, Redox and clustering of iron in silicate glasses, J. Non-Cryst. Solids 253 (1999) 203–209, https://doi.org/10.1016/S0022-3093(99)00361-0.

[37] V.C. Kress, I.S.E. Carmichael, The compressibility of silicate liquids containing Fe2O3 and the effect of composition, temperature, oxygen fugacity and pressure on their redox states, Contrib. Mineral. Petrol. 108 (1991) 82–92, https://doi.org/10.1007/BF00307328/METRICS.

[38] B. Hehlen, D.R. Neuville, D. Kilymis, S. Ispas, Bimodal distribution of si–o–si angles in sodo-silicate glasses, J. Non-Cryst. Solids 469 (2017) 39–44, https://doi.org/10.1016/j.jnoncrysol.2017.04.009.

[39] A. Quaranta, A. Rahman, G. Mariotto, C. Maurizio, E. Trave, F. Gonella, E. Cattaruzza, E. Gibaudo, J.E. Broquin, Spectroscopic investigation of structural rearrangements in silver ion-exchanged silicate glasses, J. Phys. Chem. C 116 (2012) 3757–3764, https://doi.org/10.1021/jp2095399.

[40] C. Le Losq, D.R. Neuville, P. Florian, G.S. Henderson, D. Massiot, The role of Al3+ on rheology and structural changes in sodium silicate and aluminosilicate glasses and melts, Geochem. Cosmochim. Acta 126 (2014) 495–517, https://doi.org/10.1016/j.gca.2013.11.010.

[41] B.O. Mysen, D. Virgo, F.A. Seifert, The structure of silicate melts: implications for chemical and physical properties of natural magma, Rev. Geophys. 20 (1982) 353–383, https://doi.org/10.1029/RG020I003P00353;WGROUP:STRING:PUBLICATION.

[42] M. Cassetta, B. Rossi, S. Mazzocato, F. Vetere, G. Iezzi, A. Pisello, M. Zanatta, N. Daldosso, M. Giarola, G. Mariotto, Deep-UV Raman spectroscopy: a novel heuristic method to characterize volcanologically relevant glasses on Mars, Chem. Geol. 644 (2024) 121867, https://doi.org/10.1016/j.chemgeo.2023.121867.

[43] M. Cassetta, M. Zanatta, M. Biesuz, M. Giarola, G. Mariotto, New insights about the role of Na–K ratio on the vibrational dynamics of synthetic-basalt glasses, J. Raman Spectrosc. 53 (2022) 540–549, https://doi.org/10.1002/JRS.6298.

[44] K. Falenty, S.L. Webb, Shear modulus, heat capacity, viscosity and structural relaxation time of Na2O-Al2O3-SiO2 and Na2O-Fe2O3-Al2O3-SiO2 melts, Phys. Chem. Miner. 37 (2010) 613–634, https://doi.org/10.1007/S00269-010-0362-7/FIGURES/18.

[45] D. Di Genova, K.U. Hess, M.O. Chevrel, D.B. Dingwell, Models for the estimation of Fe3+/Fetot ratio in terrestrial and extraterrestrial alkali- and iron-rich silicate glasses using Raman spectroscopy, Am. Mineral. 101 (2016) 943–952, https://doi.org/10.2138/AM-2016-5534CCBYNCND/ASSET/GRAPHIC/J_AM-2016-5534CCBYNCND_FIG_007.JPG.

[46] M. Cassetta, G. Mariotto, N. Daldosso, E. De Bona, M. Biesuz, G.D. Sorarù, R. Almeev, M. Zanatta, F. Vetere, Viscosity, boson peak and elastic moduli in the Na2O-SiO2 system, Minerals 13 (2023), https://doi.org/10.3390/min13091166.

[47] R. Jose, T. Suzuki, Y. Ohishi, Thermal and optical properties of TeO2–BaO–SrO–Nb2O5 based glasses: new broadband Raman gain media, J. Non-Cryst. Solids 352 (2006) 5564–5571, https://doi.org/10.1016/j.jnoncrysol.2006.09.013.

[48] Q. Huang, T. Liu, X. Shen, X. Li, A. Lu, Y. Gu, Characterization of Fe2O3 doping on structure, optical and luminescence properties of magnesium aluminosilicate-based glasses, J. Non-Cryst. Solids 563 (2021) 120786, https://doi.org/10.1016/J.JNONCRYSOL.2021.120786.

[49] A.K. Prasad, M. Jain, Dynamics of the deep red Fe3+ photoluminescence emission in feldspar, J. Lumin. 196 (2018) 462–469, https://doi.org/10.1016/J.JLUMIN.2017.11.051.

[50] X. Zhang, D. Chen, X. Chen, C. Zhou, P. Chen, Q. Pang, L. Zhou, Broadband near-infrared luminescence from Fe3+-activated NaScSi2O6 phosphors for luminescence thermometry and night-vision applications, Dalton Trans. 51 (2022) 14243–14249, https://doi.org/10.1039/D2DT02329F.

[51] D.V. Azamat, J. Debus, D.R. Yakovlev, V.Y. Ivanov, M. Godlewski, M. Fanciulli, M. Bayer, Ground and excited states of iron centers in ZnO: pulse-EPR and magneto-optical spectroscopy, Phys. Rev. B Condens. Matter 92 (2015), https://doi.org/10.1103/PHYSREVB.92.195202.

[52] J. Tauc, R. Grigorovici, A. Vancu, Optical properties and electronic structure of amorphous germanium, Phys. Status Solidi 15 (1966) 627–637, https://doi.org/10.1002/PSSB.19660150224.

[53] J. Tauc, Optical Properties of Amorphous Semiconductors, Amorphous and Liquid Semiconductors, 1974, pp. 159–220, https://doi.org/10.1007/978-1-4615-8705-7_4.

[54] P. Makuła, M. Pacia, W. Macyk, How to correctly determine the band gap energy of modified semiconductor photocatalysts based on UV-Vis spectra, J. Phys. Chem. Lett. 9 (2018) 6814–6817, https://doi.org/10.1021/ACS.JPCLETT.8B02892cccc.

[55] F. Urbach, The long-wavelength edge of photographic sensitivity and of the electronic absorption of solids, Phys. Rev. 92 (1953) 1324, https://doi.org/10.1103/PHYSREV.92.1324.

[56] I. Studenyak, M. Kranjčec, M. Kurik, Urbach rule in solid state physics, Int. J. Opt. Appl. 4 (2014) 96–104, https://doi.org/10.5923/j.ajcmp.26130306.01.
[57] M.A. Chaudhry, M. Altaf, Optical absorption studies of sodium cadmium phosphate glasses, Mater. Lett. 34 (1998), https://doi.org/10.1016/S0167-577X(97)00168-7.
[58] P.M. Vinaya Teja, A. Ramesh Babu, P. Srinivasa Rao, R. Vijay, D. Krishna Rao, Structural changes in the ZnF2–Bi2O3–GeO2 glass system doped with Fe2O3 by spectroscopic and dielectric investigations, J. Phys. Chem. Solid. 74 (2013) 963–970, https://doi.org/10.1016/J.JPCS.2013.02.015.
[59] P.R. Rao, L. Pavić, A. Moguš-Milanković, V. Ravi Kumar, I.V. Kityk, N. Veeraiah, Electrical and spectroscopic properties of Fe2O3 doped Na2SO4–BaO–P2O5 glass system, J. Non-Cryst. Solids 358 (2012) 3255–3267, https://doi.org/10.1016/j.jnoncrysol.2012.08.032.
[60] M.T. Nayak, J.A.E. Desa, P.D. Babu, Magnetic and spectroscopic studies of an iron lithium calcium silicate glass and ceramic, J. Non-Cryst. Solids 484 (2018) 1–7, https://doi.org/10.1016/J.JNONCRYSOL.2017.12.050.
[61] A. Bhogi, P. Kistaiah, Spectroscopic properties of alkali alkaline earth borate glasses doped with Fe3+ ions, J. Austr. Ceram. Soc. 56 (2020) 127–138, https://doi.org/10.1007/S41779-019-00426-3.
[62] H.D. Shashikala Subhashini, N.K. Udayashankar, Influence of Fe3+ ions on optical, structural, thermal and mechanical properties of Li2O–Na2O–K2O–ZnO–B2O3 based glass system, Ceram. Int. 46 (2020) 5213–5222, https://doi.org/10.1016/J.CERAMINT.2019.10.269.
[63] S.P. Singh, R.P.S. Chakradhar, J.L. Rao, B. Karmakar, EPR, FTIR, optical absorption and photoluminescence studies of Fe2O3 and CeO2 doped ZnO–Bi2O3–B2O3 glasses, J. Alloys Compd. 493 (2010) 256–262, https://doi.org/10.1016/J.JALLCOM.2009.12.075.
[64] A.N. Trukhin, J.L. Jansons, K. Truhins, Luminescence of silica glass containing aluminum oxide, J. Non-Cryst. Solids 347 (2004) 80–86, https://doi.org/10.1016/J.JNONCRYSOL.2004.08.100.
[65] L. El Mir, A. Amlouk, C. Barthou, Visible luminescence of Al2O3 nanoparticles embedded in silica glass host matrix, J. Phys. Chem. Solid. 67 (2006) 2395–2399, https://doi.org/10.1016/J.JPCS.2006.05.059.
[66] Z.Q. Yu, C.X. Wang, X.T. Gu, C. Li, Photoluminescent properties of boehmite whisker prepared by sol-gel process, J. Lumin. 106 (2004) 153–157, https://doi.org/10.1016/j.jlumin.2003.09.004.